Jurnal Tribologi 49 (2026) 148-173

MYTRIBOS
Malaysian Tribology Society

Jurnal Tribologi
Website : jurnaltribologi.mytribos.org e-issn: 2289-7232

Traction performance analysis and life prediction of elevator traction wheel based on three-dimensional point cloud reconstruction

Jian Liu [1], Haijian Wang [2], Xiaoguang Pan [1*], Xishan Zhu [1], Chengwei Ju [1], Chengwen Yu [2]

[1] Guangxi Special Equipment Inspection and research Institute, CHINA.
[2] Guangxi Key Laboratory of Manufacturing System & Advanced Manufacturing Technology, School of Mechanical and Electrical Engineering, Guilin University of Electronic Technology, CHINA.
*Corresponding author: 2115053855@qq.com

KEYWORDS

3D point cloud reconstruction
traction wheel
groove wear
traction performance
fatigue life

ABSTRACT

This study examines the influence of groove wear on elevator traction wheel performance and predicts residual fatigue life. Using 3D point cloud reconstruction, service traction wheel models with varying wear levels (0 mm, 0.18 mm, 0.31 mm, 0.72 mm) were generated. Finite element simulations and fatigue life models were employed to assess traction capacity and lifespan under operational conditions. Results show that traction force significantly increases only under dangerous (0.31 mm) and severe (0.72 mm) wear during elevator stagnation. Maximum equivalent stresses in wheel grooves rise progressively with wear, reaching 340 MPa (0 mm), 378 MPa (0.18 mm), 481 MPa (0.31 mm), and 619 MPa (0.72 mm). Corresponding residual fatigue lives decrease to 10.7, 8.5, 4.9, and 2.7 years, respectively, as calculated via fatigue life formulas. The study demonstrates that severe groove wear critically elevates stress concentrations and accelerates fatigue failure, with lifespan reductions exceeding 60% at maximum wear. These findings provide a quantitative framework for evaluating traction performance degradation and establishing maintenance thresholds for worn traction wheels. The integrated approach combining 3D reconstruction, stress analysis, and fatigue modeling offers an effective technical solution for predictive maintenance in elevator systems.

Received 28 April 2025; received in revised form 26 May 2025; accepted 4 Jun 2025.
To cite this article: Liu et al. (2026). Traction performance analysis and life prediction of elevator traction wheel based on three-dimensional point cloud reconstruction. Jurnal Tribologi 49, pp.148-173.

1.0 INTRODUCTION

The elevator traction wheel is a core component of an elevator traction system, and its performance is directly related to the safety and reliability of the elevator. The traction wheel depends on the friction between the traction wire rope and the wheel groove to drive the elevator up and down; however, if this traction persists for a long time, it will lead to groove wear of the traction wheel. When the wear reaches a certain degree, the structure of the wheel groove changes, which significantly affects the traction performance of the elevator and reduces the service life of the traction wheel. Therefore, three-dimensional (3D) point cloud reconstruction technology is used to obtain the wheel groove structure model of the traction wheel. Additionally, it is used to study and analyze the traction performance of the traction wheel with different wear degrees under different working conditions. We combine the finite element simulation analysis method and fatigue life prediction model to predict the residual fatigue life of the traction wheel, which is crucial for monitoring the traction performance of the traction wheel and ensuring the safety of the elevator.

In the 1970s, some European and American countries began to develop laser-scanning technology, and Professor Ackermann organized the development of the world's first laser measurement system in 1980 (Xu et al., 2008). In 2000, the University of Washington applied 3D scanning technology to large-scale sculptures to obtain point-cloud information and digitalize cultural heritage (Wang et al., 2010). China has also developed rapidly in this field, and several laser scanning system R&D companies, such as North Science and Technology, Deep Vision Intelligence, and the Haida Number Cloud have emerged. Subsequently, the original collected point cloud is denoised and reduced. Taubin et al. proposed an isotropic algorithm based on the Laplacian operator to achieve linear and fast denoising (Taubin, 1995); however, the isotropy could not retain the detailed features of the object model. Fleishman et al. combined the bilateral filtering algorithm in image processing and proposed a method based on filtering the normal direction of the mesh vertices in the local domain (Fleishman et al., 2003); however, it could not handle irregular mesh models. Zhang et al. combined global variables and a piecewise constant function space to achieve denoising of the triangular mesh, which better preserved the edge-point cloud data but did not guarantee convergence (Zhang et al., 2015). The above grid-based point-cloud denoising method has been studied for decades, but some noise is introduced in the initial grid division stage; therefore, another direct denoising method based on point clouds is gradually increasing. Wang et al., 2016 adopted a geometric similarity algorithm to improve the operational efficiency of the algorithm while retaining the effective feature points of the point cloud mode. Tao et al., 2018 divided noise points into discrete and non-discrete points and proposed density clustering and voting discrimination methods based on point clouds for denoising. Zou et al., 2020 obtained the optimal distance between two points using particle swarm optimization, smoothed point-cloud data using wavelet processing and retained the edge features of the point cloud using Gaussian filtering. Zhu et al., 2012 proposed the calculation of feature points based on the Hausdorff's distance of the principal curvature of the point cloud data. They retained certain feature point cloud data and removed point clouds without obvious features to simplify the point cloud data. Three-dimensional reconstruction algorithms can be divided into mesh, display, and implicit surface reconstruction algorithms. The mesh surface reconstruction algorithm represents the surface model of the target object based on grids of different shapes formed between the point clouds in space. Ma, 2011 proposed a mesh surface reconstruction algorithm based on Delaunay triangulation to prioritize point-cloud data and determine the feature grid with the best shape. It can effectively reconstruct sharp features of the target object without requiring additional processing to fill the holes. proposed a generalized regularization term to improve the point-cloud reconstruction algorithm, which can ensure the smoothness of the flat region even under the interference of cloud noise and enhance the rendering effect of point clouds in the process of visual interaction, thus improving the user's sense of experience. The display surface reconstruction algorithm based on parameterization first parameterizes the point cloud and then calculates the surface equation parameters according to known functions so that the reconstructed surface is close to the real surface of the target object. Li et al., 2006 proposed a reconstruction method to fit a topological surface with parameterized surfaces and initialized the surface parameters after generating a grid from point-cloud data. The square distance function is defined as the degree of error, and the target model is approximated iteratively. Aiming at models with complex topological surfaces based on the nonuniform rational B-spline algorithm (NURBS), Zhang et al. proposed a 3D reconstruction algorithm based on the overall parameters of point-cloud data, which improved the accuracy and efficiency of the reconstruction method (Zhang et al., 2017). The implicit surface reconstruction algorithm can generate topological surfaces with arbitrary shapes by constructing implicit surface functions to fit 3D point clouds and is suitable for target objects with complex surfaces. Savchenko et al. used radial basis functions to fit the point clouds (Savchenko et al, 1995). As global support was required to calculate implicit surfaces, the solved linear system became dense and unsuitable for the surface reconstruction of large-scale point cloud data. To realize the 3D reconstruction of large-scale point clouds, Morse et al. used Wendland's compact supported radial basis function to sparsify the linear system and expand the adaptive range of the algorithm (Morse et al., 2001).

Shi et al., 2021 developed a precise measurement device to assess the groove profile of traction sheaves and utilized computer simulations to analyze workpiece images, enhancing the accuracy of groove wear value determination. Wang et al., 2021 examined acoustic emission signals from four sensors during traction sheave operation with varying wear levels, effectively distinguishing between signals to precisely assess sheave wear. Papas et al., 2022 employed 3D digital scanning on elevator traction sheaves to generate CAD models for stress analysis, uncovering elevated stress levels at the sheave groove through static and dynamic behavior assessment. While research on elevator traction sheaves is limited, studies on similar friction wheels offer valuable insights. For example, Bošnjak et al., 2016 investigated the horizontal characteristics of rope cyclic loads and evaluated the combined impact of mean stress and alternating stress in critical pulley areas under typical loading conditions using finite element analysis.

In the 20th century, Paris et al., 2009 proposed the Paris formula, a seminal contribution that transformed fatigue life prediction by elucidating crack propagation mechanisms within the framework of fracture mechanics theory. Li et al., 2019 devised a predictive approach centered on adaptive parameter tuning of physical models, leveraging least squares optimization to adjust crack propagation model parameters for rolling bearings, thereby enhancing the accuracy of crack growth life forecasts. Birt et al., 2006 observed, through constant-stress accelerated degradation experiments, a direct association between degradation rates and temperature elevation. Subsequently, the Arrhenius model was employed to characterize degradation parameters and forecast the average lifespan. Molent et al., 2003 conducted a comparative analysis of regression models for fitting crack data in aircraft wing panels, ultimately advocating for the efficacy of exponential regression models in predicting crack propagation trends in these structural components.

Conventional methods for detecting wear on traction sheave grooves primarily rely on two-dimensional images or manual visual inspections, which may not fully characterize the three-dimensional topography of the sheave. By utilizing laser scanning or structured light imaging to capture high-precision 3D point cloud data, it is possible to accurately reconstruct the three-dimensional geometric features of the sheave surface, effectively capturing subtle wear patterns like localized pitting and edge wear. This approach significantly improves the comprehensiveness and accuracy of inspections. Consequently, employing 3D point cloud reconstruction technology to generate structural models of the sheave grooves, coupled with assessing traction performance under various wear levels and operational conditions, as well as utilizing finite element simulation analysis and fatigue life prediction models, allows for a reliable estimation of the remaining fatigue life of traction sheaves. This methodology is crucial for monitoring the performance of traction sheaves and ensuring elevator safety.

2.0 ACQUISITION AND RECONSTRUCTION OF 3D POINT CLOUD DATA OF TRACTION WHEEL

2.1 Experimental Platform Construction

Based on the scanning requirements of the wheel groove of the traction wheel, a 3D ray scanner was selected as the scanning tool for the experimental bench, and a system test bench for the wheel groove scanning of the elevator traction wheel was built (Figure 1). The experimental platform was composed of a traction wheel support frame, an upper computer system, an encoder control board, a line laser scanner, a traction wheel, a frequency converter, a rotary encoder, and a three-phase alternating current motor.

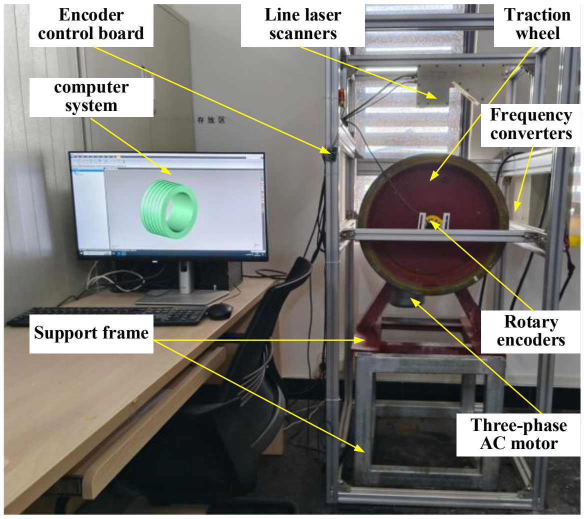

Figure 1: Point cloud scanning test bench of traction wheel.

A CA-HL02MX line scanner (Keyence Corporation) was used in this study. Its working principle involves projecting auxiliary light onto a target object and capturing 3D information by analyzing the reflected light signals. This noncontact measurement system achieves high-accuracy scanning of complex curved surfaces, offering high-resolution precision and exceptional adaptability for dark-colored components. Figure 2 shows a schematic representation of the detection mechanism.

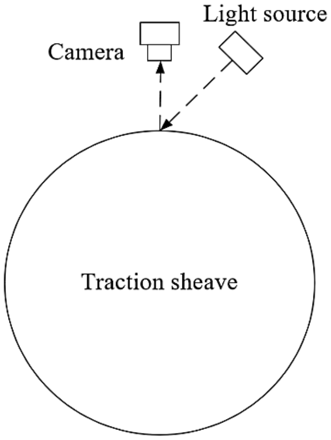

Figure 2: Schematic of the scanner's measurement principle.

2.2 Traction Wheel Point Cloud Data Acquisition and Processing

A mark was attached to the side of the traction wheel, and the speed adjustment button of the frequency converter was used to enable the traction wheel to rotate at a slow and consistent pace. Once the line laser crossed the marked position, the scanning process began. Simultaneously, the rotary encoder started counting. When the line laser crossed the marked position for the second time, the scanning halted, and the rotary encoder immediately stopped counting. The data gathered at this moment represents the point-cloud data for one complete rotation of the traction wheel. Subsequently, the acquired point-cloud data in txt format were fed into the point-cloud processing software. Figure 3(a) shows the image formed after importing 100% of the traction wheel point-cloud data. The numbers of point clouds imported at 100%, 50%, and 33% ratios were 2,123,983, 1,061,991, and 713,097, respectively. Among these, 100% yielded the largest number of imported point clouds. Although it offers the highest point-cloud density, it also brings in a substantial number of stray and noisy points, increasing the load on computer resources. However, a 33% ratio resulted in a relatively small number of imported point clouds with low data density, leading to extensive blank areas in the point-cloud model, which severely impacted the subsequent modeling accuracy. After a comprehensive comparative analysis, a 50% ratio was selected to import the original data. This ratio prevents excessive consumption of computer resources and ensures that the density of the point clouds meets the demands for subsequent fine-scale modeling.

To address the lack of RGB information in text-formatted point-cloud data, this study employed a point-coloring algorithm to optimize the color of the point cloud. Based on the geometric features of the traction wheel, a curvature-adaptive point-cloud simplification strategy was adopted. This strategy retains the original point-cloud density in regions with high curvature variation rates and performs point-cloud sparsification in flat areas, effectively balancing the need for data-scale reduction and feature preservation.

For nonconnected and isolated points in the original point cloud, an outlier detection algorithm with three iterations of filtering was applied, removing 224,558 isolated points and retaining 837,433 effective points. After point cloud processing was completed, the Delaunay triangulation algorithm was used to construct the topological relationships between the points, with a mesh density of 579,463 facets and a high-quality threshold set to high.

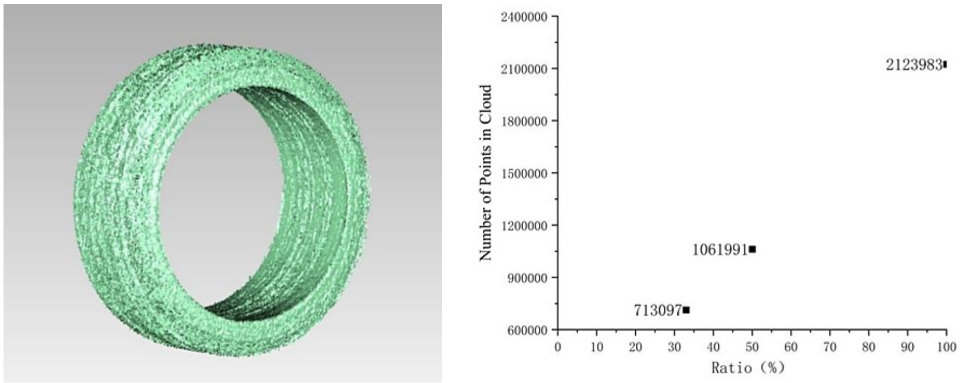

(a) (b)

Figure 3: Relationships between the numbers of point clouds imported at different ratios. (a) Point cloud image of the 100% ratio; (b) Quantitative relationships of point clouds at different ratios.

In the mesh-processing stage, the core tasks include hole filling and surface smoothing. Common hole-filling strategies can be categorized into three types: full-hole filling, bridging segmentation, and partial hole filling. Considering that the traction wheel mesh model is a rotational body with a large central hole required to maintain the structural integrity, the curvature-based full-hole filling method is not applicable. The repair process should follow the "small-to-large" principle: prioritize the treatment of small holes, and then gradually fill larger holes after the smaller ones are repaired. For small single holes, a curvature-based partial filling method can be used; if the hole size is too large, bridging techniques can be used to divide it into several subregions for step-by-step filling. Surface smoothing is more complex and requires differentiated strategies based on the geometric features of different regions of the model (such as curvature and concavity/convexity). First, the LASSO tool was used to locally select concave and convex areas and to apply the feature removal command for initial surface smoothing. Subsequently, a spike-removal tool was used to detect and eliminate sharp protrusions, followed by a relaxation tool to further optimize the mesh topology. This process was iterated until the preset accuracy standard is achieved, and the entire model was subjected to global detection and residual defect repair using the mesh repair command.

2.3 3D Materialization of the Traction Wheel

Reconstructing the surface of the traction wheel model after improving its quality is crucial. In this study, a surface interpolation reconstruction method based on the NURBS was selected. The interpolated curve determined by the interpolation function must pass through all type value points to guarantee a zero error between the fitted curve and the real data point. Curves were drawn from the traction wheel point cloud data. These curves are used to define the outline of the traction wheel shape. An intersection may exist between the curves generated for the first time, and the vertices of the contour can be controlled to separate and move to suitable positions to ensure that the layout of the curve satisfies the design requirements of the reconstruction target. When the above operation fails to lay out the contour well, it is necessary to continue optimizing the surface quality of the incorrect position and re-extract the contour. This process was repeated until each extracted contour line became concise and clear. Even if there is no problem with intersecting contour lines, it is necessary to check whether each slot in the traction wheel model is covered by contour lines. The contour-line extraction of the traction wheel is shown in Figure 4(a).

In the generation and fitting of the March curve surface, the automatically generated surface sheet generally cannot meet the final quality requirements. Therefore, its distribution must be made more uniform using rearrangement and relaxation commands. The grid construction command was used to select an appropriate graph resolution based on the required model accuracy. The selected grid graph resolution is 30, and the intersection points between the grids are adjustable control points. The connection points of the grid structure must be checked and optimized, as the quality of the surface is checked. Figure 4(b) shows the generated traction-wheel grid structure.

Finally, the NURBS surface generation function was used to select the number and tolerance of the control vertices, complete the model reconstruction of the traction wheel, and derive the appropriate model format according to the requirements of subsequent analysis. Figure 4(c) shows the final reconstructed 3D traction wheel model.

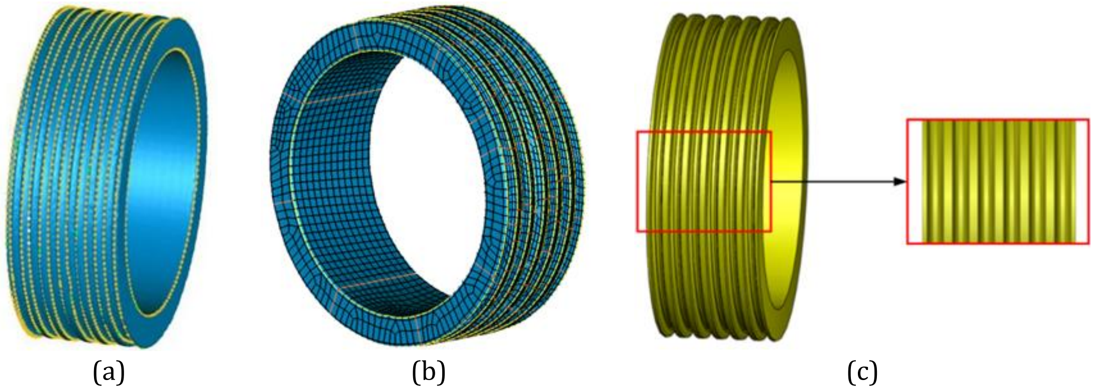
(a) (b) (c)

Figure 4: Contour extraction and 3D reconstruction of traction wheel. (a) Contour extraction; (b) Lattice structure; (c) Reconstruction model.

The 3D modeling based on point-cloud data depends on the surface model of the target. There was some deviation between the final 3D model and reconstructed surface model in the actual fitting process. Generally, after model reconstruction, a model deviation analysis is performed to check whether the reconstructed results meet the accuracy requirements. The tractive performance and residual life analyses can be performed based on the reconstructed tractive wheel model only when the requirements are met.

The processed traction wheel surface model and reconstructed 3D solid model were imported into Geomagic Control X software, and the reconstruction deviation was analyzed based on the original data. First, the coordinates of the two models were aligned, the deviation analysis method of point cloud comparison was selected, and the calculated parameters such as tolerance and sampling density were adjusted to balance the accuracy and efficiency of the calculation. Using the visualization tool provided by the software, the deviations between the models were viewed using a color graph. Compared to some acquisition objects with irregular shapes, the accuracy of the point cloud data collected in this project is higher. Figure 5 shows the deviation distribution diagram obtained after the deviation analysis of the model.

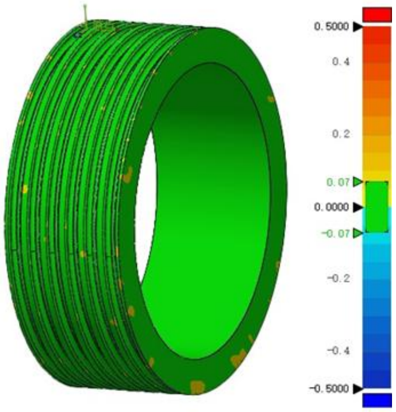

Figure 5: Deviation analysis cloud diagram.

The deviation distribution diagram of the traction wheel model shows that the deviation range of the model is -0.088 mm to +0.135 mm, and the average deviation is 0.0167 mm. The accuracy of the reconstructed model reaches 94.8% within the tolerance range of ±0.07 mm, and the overall accuracy is high. The analysis results suggest that the main reason for the biggest deviation is that the internal curve of the wheel groove of the traction wheel is more complicated than the external contour. Owing to problems such as shading or rusting when the scanner collects the original data, the data could not be completely collected. Therefore, holes were repaired during the point and polygon processing stages. Therefore, there are some errors between the final model and the 3D point cloud, but the final accuracy still meets the requirements of 3D fine modeling.

3.0 ANALYSIS OF TRACTION PERFORMANCE OF TRACTION WHEEL WITH DIFFRENT WEAR DEGREES

3.1 Analysis of Wear Characteristics of Elevator Traction Wheel

The upward and downward movements of the traction elevator are accompanied by friction between the traction wheel and the wire rope. The elevator operation has an appropriate traction force to avoid accidents caused by insufficient or excessive traction force only when the friction between the traction wheel and wire rope meets the requirements. The friction contact area between the wire rope and traction wheel is the groove part of the traction wheel, and the geometric feature size of the traction wheel determines its traction capacity. With increasing friction time, the groove of the traction wheel will have a certain wear, the geometric feature size of the groove will change, and the traction gravity of the traction wheel will also be affected; therefore, analyzing the structure of the traction wheel groove is essential. The main traction wheel groove structure included a semicircular groove with a notch, a V-shaped groove with a notch, and a semicircular groove. Fig. 6 shows the three-groove structure.

The semicircular groove with a prefabricated notch at its base facilitates partial wedging of the wire rope, inducing elastic deformation to enhance contact pressure. This design results in an increased friction coefficient of 1.5-2 times compared to conventional semicircular grooves. In cases of groove wear, the wire rope settles into the notched position, maintaining consistent friction characteristics and preventing abrupt declines in traction capacity due to wear.

Conversely, the V-shaped groove with notches exerts compression forces on the wire rope, leading to a higher friction coefficient than standard semicircular grooves but lower than notched semicircular grooves. As wear progresses, the groove profile transitions towards that of a notched semicircular groove, leading to a rapid reduction in friction and necessitating frequent tension adjustments. Standard semicircular grooves offer the largest contact area and lowest specific pressure, resulting in the lowest equivalent friction coefficient and weakest traction capacity.

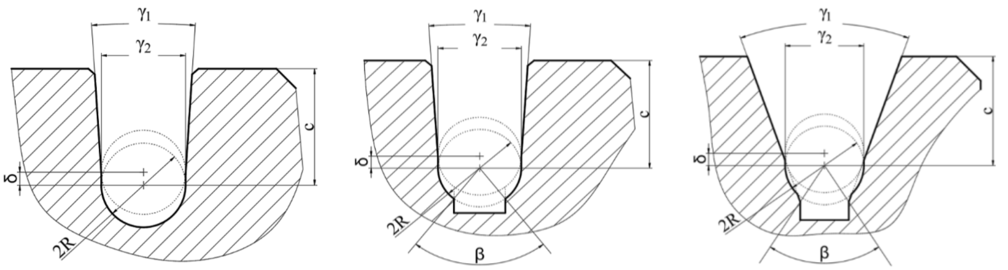

(a) (b) (c)

Figure 6: Groove structure diagram. (a) a semi-circular groove; (b) a semi-circular groove with a notch; (c) a V-shaped groove with a notch.

We examined the semi-circular wheel groove with a cut. As the cross-section of the wire rope is a fitting circle consistent with the shape of the wheel groove, assuming that the surface of the wire rope is not worn, the size of the fitting circle remains unchanged. When the friction and wear between the wire rope and the wheel groove occurs, the depth of the wheel groove increases and the height of the bottom cut decreases continuously. The wear depth of a semi-circular groove with a notch is δ, the opening angles before and after the groove wear are respectively γ_1 and γ_2, and the radius of the wire rope is R. Based on the structure of the semi-circular groove with a notch, the relation of the opening angle change can be obtained as follows:

$$\gamma_2 = \gamma_1 - 2\arccos\frac{R - \delta \cdot \sin {}^{\gamma_1}\!/_{2}}{R} \tag{1}$$

With continuous wear of the wheel groove, the tangent points of the wire rope and wheel groove continued to decrease, and the opening angle of the wheel groove continued to decrease. Assuming that only the change trend of the shape of the wheel groove with the wear is considered, when the wear reaches a certain degree, the opening angle of the wheel groove is reduced to 0, and further wear cannot affect the size of the opening angle. The corresponding wear depth δ can be expressed by Equation (2).

$$\delta = R \cdot \frac{1 - \cos {}^{\gamma_1}\!/_{2}}{\sin {}^{\gamma_1}\!/_{2}} \tag{2}$$

According to the elevator safety manual, the vertical distance between the bottom end of the wire rope and the bottom of the incision should not be less than 1 mm so that the traction wheel will not cause safety problems owing to excessive wear of the wheel groove. Generally, the wear degree of the wheel groove can be divided into four grades: slight, safe, dangerous, and severe wear. The wear range corresponding to each wear grade is introduced below.

A traction wheel model 520-6-13 was scanned in this study. Table 1 lists the elevator traction system. Figure 7 shows a schematic of the elevator system.

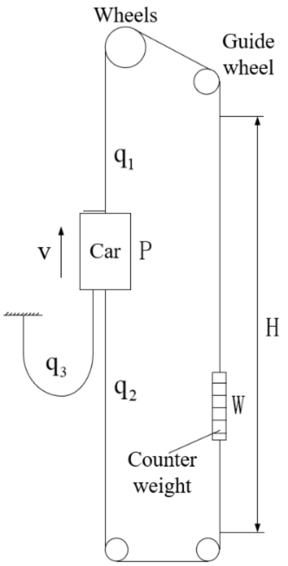

Figure 7: Schematic of elevator traction system.

Table 1: Parameters of elevator traction system.

Parameter name	Parameter representation	Unit	Parameter value
Car weight	P	kg	1200
Rated speed	V	m/s	2
Rated deadweight	Q	kg	1000
Equilibrium coefficient	K	%	0.46
Lift height	H	m	35
Traction ratio	I	—	1
Wire rope number	n_1	Root	6
Wire rope diameter	D	mm	12
Mass per unit length of wire rope	q_1	kg/m	0.61
Compensating chain roots number	n_2	Root	1
Mass per unit length of compensated chain	q_2	kg/m	3
Accompanying cables number	n_3	Root	1
Mass per Unit Length of Trailing Cable	q_3	kg/m	0.9
Envelope angle	A	degree	160
Opening angle	Γ	degree	50
Lower notch angle	B	degree	100

In this system, W denotes the elevator counterweight, which can be expressed as:

$$W = P + kQ \tag{3}$$

Table 1 shows that the diameter of the wire rope (D) is 12 mm, the radius of the wire rope (R) is 6 mm, and the cut angle of the lower part of the wheel groove (β) is 100°. To ensure the safety of the elevator, the groove opening angle is generally not less than 25°. According to Equations (1) and (2), when the groove opening angle γ of the traction wheel is reduced to 25° and 0°, the wear amount δ of the groove is 0.66 mm and 1.33 mm, respectively. In the initial case, the height of the groove cut L was 5 mm, and the height h from the bottom end of the wire rope to the bottom surface of the cut was calculated using Equation (4).

$$h = L - (R - R \cdot \cos\frac{\beta}{2}) \tag{4}$$

In the initial case, the height h from the bottom end of the wire rope to the bottom surface of the incision is 3.05 mm, and the vertical distance from the bottom end of the wire rope to the bottom surface of the incision based on the above elevator safety regulations shall not be less than 1 mm. Thus, the allowable variation range of wear depth δ based on this condition is 0–2.05 mm.

Combined with the wear curve characteristics of the material, the quantitative expression results for the wear degree of the wheel groove are presented in Table 2.

Table 2: Quantitative expression of wear degree.

Wear grade	Light wear	Safety wear	Dangerous wear	Heavy wear
Range of δ	0–0.15mm	0.15–0.66mm	0.66–1.33mm	1.33–2.05mm

3.2 Analysis of the Relationship between Drag Coefficient and Wheel Groove Wear Degree

Based on the “Elevator Manufacturing and Installation Safety Technical Specifications” (hereinafter referred to as GB7588.2-2020), the size of the elevator’s traction capacity can be expressed through the traction coefficient G as follows:

$$G = e^{f\alpha} \tag{5}$$

In Equation (5), G represents the traction coefficient of the elevator; f represents the equivalent friction factor; and α indicates the size of the wrap angle of the wire rope on the wheel groove.

The equivalent friction coefficient f of the traction wheel is related to the shape and friction coefficient of the wheel groove, and the shape difference of the wheel groove is primarily reflected in the size of the groove opening angle γ and the bottom notch angle β. f is expressed as follows:

$$f = \mu \cdot F(\gamma, \beta) \tag{6}$$

In Equation (6), μ represents the friction coefficient, and the size is determined by different working conditions.

The expression for this function also differs for different types of wheel grooves. For the semi-circular wheel grooves with notches investigated in this study, the specific expressions are as follows:

$$F(\gamma,\beta)=\frac{4\left(\cos\frac{\gamma}{2}-\sin\frac{\beta}{2}\right)}{\pi-\gamma-\beta+\sin\gamma-\sin\beta} \tag{7}$$

The size of the equivalent friction coefficient is jointly affected by β and γ. If the diameter wear of the wire rope is not considered to be smaller, the impact of wear on the shape of the wheel groove is reflected by the opening angle γ, and the impact on the incision angle β of the wheel groove can be ignored. β can be regarded as a constant, according to Table 1, and the initial angle value of β is 100°. Converted to radians (1.75 radians), function F becomes a relation for the opening angle γ.

$$F(\gamma)=\frac{4\left(\cos\frac{\gamma}{2}-0.77\right)}{\pi-2.73-\gamma+\sin\gamma} \tag{8}$$

The curve of the function at this point is shown in Figure 8.

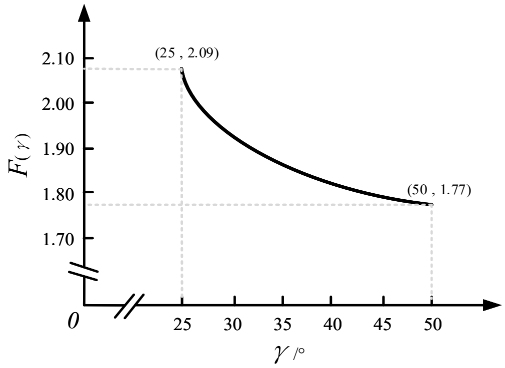

Figure 8: Graph of function $F(\gamma)$.

When the β is constant, the function F increases with decreasing γ, and the traction capacity of the wheel groove also increases. To avoid the phenomenon of excessive traction capacity leading to the occurrence of the elevator top, the regulation of the wheel groove opening angle γ value is not allowed to be less than 25°. Additionally, the discussion above also suggests that, as the wear amount δ of the wheel groove increases, the opening angle γ of the wheel groove continues to decrease. When the wear amount reaches 1.33 mm, the opening angle of the wheel groove decreases to 0° and no longer changes. Therefore, when the wear amount is less than 1.33 mm, the function F value continues to increase with the wear degree, and eventually, the friction coefficient f of the wheel groove increases. However, after the wear amount reaches 1.33 mm, the function F value does not change; therefore, the friction coefficient f of the wheel groove did not change.

Based on the requirements of GB7588.2-2020, when the wheel groove is worn, the package angle is calculated using the following geometric relationship:

$$\alpha = 4.71 - \arctan\frac{W}{H} - \arccos\left(\frac{D-2\delta-d}{2\sqrt{W^2+H^2}}\right) \tag{9}$$

In Equation (9), W represents the horizontal axis distance between the traction wheel and the guide wheel; D represents the pitch circle diameter of the traction wheel; H represents the vertical axis distance between the traction wheel and the guide wheel; d represents the pitch circle diameter of the guide wheel.

The size of the envelope angle is related to the relative position between the traction and guide wheels, as well as to the initial pitch circle diameter. The maximum wear δ of the wheel groove does not exceed 3 mm, and the horizontal axis distance W and vertical axis distance H between the traction wheel and the guide wheel are considerably larger than the maximum wear. After the elevator traction system is installed, the values of W and H do not change; that is, the wear amount of the wheel groove cannot significantly affect the envelope angle α. Therefore, the small change of the envelope angle caused by the wheel groove wear cannot affect the elevator's traction ability; it can be ignored.

3.3 Traction Performance Analysis based on a 3D Solid Model of the Traction Wheel

After exploring how wear affects the traction performance of the traction wheel, the above point cloud data acquisition and 3D model reconstruction process were performed on a 520-6-13 type traction wheel with different degrees of wear, and the wheel groove opening angle after wear was measured. The diameter D of the wire rope and initial wheel groove opening angle are known. According to Equation (1), the wear δ of multiple reconstructed traction wheel models was calculated, as shown in Table 3.

Table 3: Wear amount of different traction wheel models.

Wheel groove opening angle γ_2 (°)	**Wear loss δ (mm)**	**Wear grade**
35.73	0.11	Light wear
26.01	0.31	Safety wear
13.35	0.72	Dangerous wear
0	1.53	Heavy wear

After measuring the parameters of the tractor wheel through the 3D reconstruction model, assuming the friction coefficient μ=0.1 (National Standard of the People's Republic of China, 2003), the equivalent friction coefficient f of the tractor wheel can be calculated according to Equations (6) and (7). Table 1 shows that the envelope angle α of the tractor wheel is 160°; the traction coefficient G of the tractor wheel can be calculated using Equation (5). Figure 9 shows the equivalent friction coefficient f and size of the drag coefficient G corresponding to the wear amounts of the four different reconstructed wear grades.

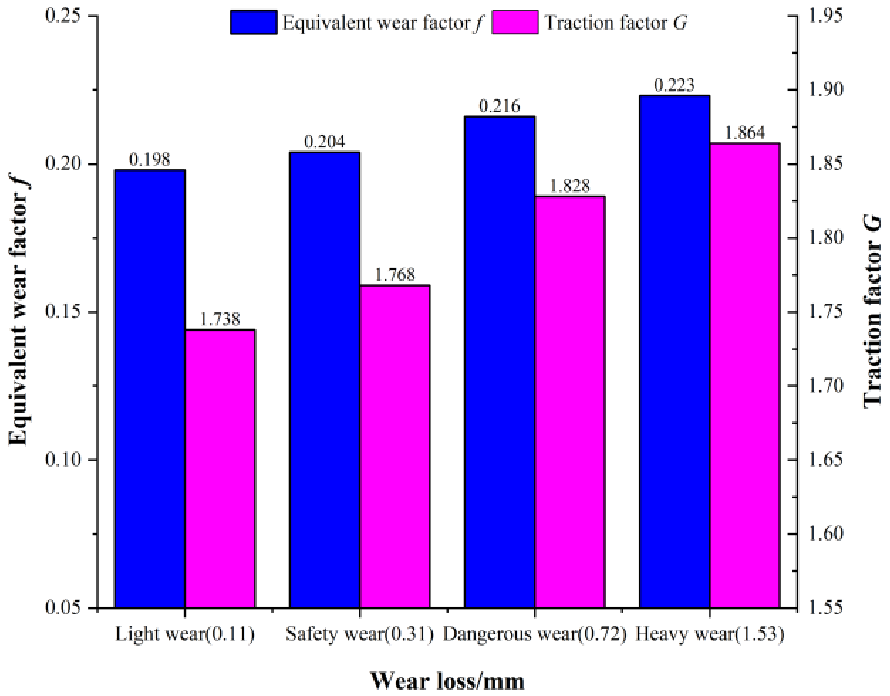

Figure 9: Equivalent friction coefficient f and drag coefficient G for different wear grades.

With an increase in the degree of wear, the equivalent friction and drag coefficients of the elevator traction wheel gradually increase; however, in the elevator operation process, it is not necessary to increase the drag coefficient. It is necessary to test whether the traction ability of the traction wheel meets the safety requirements of the elevator to ensure that the steel wire rope and traction wheel do not slip under the condition of static balance. To ensure that the elevator has sufficient traction capacity to drive the car up and down, the following traction conditions must be met:

$$\begin{cases} \dfrac{T_1}{T_2} \le e^{f\alpha}, & \text{braking conditions} \\ \dfrac{T_1}{T_2} \ge e^{f\alpha}, & \text{retention condition} \end{cases} \tag{10}$$

In Equation (10), T_1 and T_2 are the tensions on the rope on both sides of the traction wheel, where T1 is the larger value and T2 is the smaller value.

According to the requirements of GB7588.2-2020, in the safety test of the elevator's traction capacity, the tension ratio on both sides of the wire rope must be calculated based on the working conditions, and the friction coefficient μ is different under different working conditions.

Under the car-loading conditions, T_1 and T_2 should be calculated when the car is at the bottom of the elevator shaft and has a rated load of 125%. The formula is as follows:

$$\begin{cases} T_1 = g_n\left(\dfrac{P+1.25Q}{i}+q_1n_1H\right) \\ T_2 = g_n\dfrac{P+kQ+q_2n_2H}{i} \end{cases} \tag{11}$$

In Equation (11), g_n denotes the acceleration of gravity; P represents car weight; Q indicates rated load capacity; i is the drag ratio; q_1 denotes the mass per unit length of the wire rope; n_1 indicates the number of wire ropes; H represents lift height; k denotes equilibrium coefficient; q_2 represents the mass per unit length of the compensation chain; and n_2 represents the number of compensating chain roots.

The friction coefficient μ under this working condition is 0.1; therefore, the lift traction coefficient G is 1.738, 1.768, 1.828, and 1.86.

Under emergency braking conditions, T_1 and T_2 should be calculated when the car is in the most dangerous position during operation, which is generally divided into two situations. First, the no-load car runs upward at the rated speed, and emergency braking is performed near the top. Second, the fully loaded car runs down at the rated speed, and emergency braking occurs when it approaches the bottom layer.

The formula for the first case is as follows:

$$\begin{cases} T_1 = \dfrac{(P+kQ)(g_n+a)}{i}+q_1n_1H(g_n+ia) \\ T_2 = \dfrac{(P+q_2n_2H+0.5q_3n_3H)(g_n-a)}{i} \end{cases} \tag{12}$$

The formula for the second case is as follows:

$$\begin{cases} T_1 = \dfrac{(P+Q)(g_n+a)}{i}+q_1n_1H(g_n+ia) \\ T_2 = \dfrac{(P+kQ+q_2n_2H)(g_n-a)}{i} \end{cases} \tag{13}$$

In Equations (12) and (13), a represents braking deceleration; q_3 represents the mass per unit length of the accompanying cable; n_3 indicates the number of accompanying cables. Under this working condition, the friction coefficient μ is calculated as follows:

$$\mu = \frac{0.1}{1+\dfrac{v}{10}} \tag{14}$$

In Equation (14), v represents the rated speed of the car. The calculated friction coefficient μ is 0.083; hence the lift traction coefficient G is 1.582, 1.605, 1.650, and 1.677, respectively, based on the wear grade.

Under the car retention condition, the traction machine rotated along the direction of the car moving up, such that the empty car hit the top. The equations for calculating T_1 and T_2 are as follows:

$$\begin{cases} T_1 = \dfrac{g_n}{i}\left(\dfrac{P+Q+q_2n_2H}{i}+0.5q_3n_3H\right) \\ T_2 = g_nq_1n_1H \end{cases} \tag{15}$$

Under this working condition, the friction coefficient μ is 0.2 (National Standard of the People's Republic of China, 2003), and the lift traction coefficient G is 3.022, 3.125, 3.342, and 3.475, respectively, based on the wear grade.

The tension ratio T_1/T_2 on both sides of the wire rope under different working conditions can be calculated by replacing the elevator parameters in Table 1. Whether the traction wheel meets the test conditions of the elevator traction performance can be determined according to different wear grades. Table 4 lists the test results for the traction wheel with different degrees of wear under different working conditions.

Table 4: Comparison of drag coefficient and pull ratio of traction wheel with different wear degrees under different working conditions.

Different conditions	Degree of wear			
	Light wear	Safety wear	Dangerous wear	Heavy wear
Car loading condition	T_1/T_2<G	T_1/T_2<G	T_1/T_2<G	T_1/T_2<G
Upward braking condition	T_1/T_2<G	T_1/T_2<G	T_1/T_2<G	T_1/T_2<G
Downward braking condition	T_1/T_2<G	T_1/T_2<G	T_1/T_2<G	T_1/T_2<G
Car retention condition	T_1/T_2>G	T_1/T_2>G	T_1/T_2<G	T_1/T_2<G

According to the elevator traction ability test standard stipulated by GB7588.2-2020, the first three working conditions can test for insufficient elevator traction ability, whereas the car retention condition can test for excessive elevator traction ability. Equation (9) and Table 4 show that, with the increase in the wear of the wheel groove of the traction wheel, in the first three working conditions, the pull ratio on both sides of the wire rope is less than the traction coefficient; that is, the traction force of the elevator is sufficient to drive the elevator to run up and down. Under the condition of car retention, the traction force provided by the traction wheel with slight wear and safe wear degree also meets the elevator inspection standards. However, the traction force provided by the traction wheel with dangerous wear and severe wear degree is overly large, which may cause the elevator topper accident. This is because the traction wheel wear causes the wheel groove opening angle to be less than the safety regulation of 25°, and the elevator traction capacity is extremely large. In real life, traction elevators also cause car fall accidents caused by insufficient traction force, and the magnitude of the traction force is determined by the friction between the wheel groove and the wire rope. Therefore, after excluding the cause of traction wheel groove wear, the elevator's insufficient traction force may be related to the change in tension inside the wire rope.

4.0 FINITE ELEMENT ANALYSIS AND RESIDUAL LIFE PREDICTION OF TRACTION WHEEL

4.1 Pre-processing of Finite Element Analysis

An actual traction wire rope typically exhibits a circular strand structure. When the elevator is running, the internal mechanical condition of the wire rope itself is very complex. When it is in contact with the groove of the traction wheel, the surface of the wire rope is not completely smooth, and there is a small gap between the contact surfaces, which causes a sudden change in the contact force in the simulation process. Therefore, in designing the wire rope model, we assumed that it had a solid cylindrical structure with a smooth surface.

As the traction wheel is generally a multi-slot structure, under normal circumstances, each traction rope in the wire rope group is the same, and the contact situation with each wheel groove should be consistent; therefore, the problem of nonuniform wear of each wheel groove is not considered. Thus, the six-slot wheel obtained by 3D reconstruction can be simplified into a single-slot wheel and assembled with one of the rope groups of the traction rope, which can meet the simulation requirements, save computing resources, and improve the quality of the grid model and analysis efficiency. Under the principle of controlling the size of the model and removing insignificant details in the model, such as the holes on the side of the traction wheel and keyway, the simplified model includes a single-slot traction wheel and a wire rope. Figure 10 shows the 3D model assembly drawing of the traction wheel and wire rope.

Figure 10: Three-dimensional model assembly drawing of traction wheel and wire rope.

Material Settings for Traction Sheave and Steel Wire Rope. The steel wire rope used in this study is type 13-6×19S-FC, with a density of 6.24×10^{-9} t/mm^3, Young's modulus of 1.43×10^5 MPa (Wu et al., 2003), and Poisson's ratio of 0.26. The traction sheave is made of QT-600-3 nodular cast iron, exhibiting a density of 7.12×10^3 kg/m^3, Young's modulus of 1.69×10^{11} Pa, Poisson's ratio of 0.286, and hardness specifications of 240–245 HB. The material parameters of the steel wire rope and the traction sheave are listed in Tables 5 and 6, respectively.

In order to ensure the precision and dependability of finite element simulation outcomes, this research employs a progressive mesh refinement approach to perform mesh independence validation for the contact interface between the steel wire rope and traction sheave. The mesh resolution for the main body of the traction sheave was designated as 12 mm, while the initial mesh resolution in the contact region was 10 mm, followed by subsequent refinement at intervals of 1 mm. Using a wear depth of .72 mm on the traction sheave as a reference, Figure 12(a) depicts the correlation between mesh resolution and maximum equivalent stress, while Figures 12(b) and 12(c) display the mesh configurations. As the mesh density in the contact area reached 8 mm, the stress fluctuation decreased to a mere 1%. Consequently, an 8 mm mesh density was ultimately chosen for the contact region to strike a balance between simulation precision and computational efficiency.

Table 5: Material parameters of wire rope.

Material	**High quality carbon steel**
Young’s modulus	1.43×10^5 MPa
Density	6.24×10^9 g/mm^3
Poisson’s ratio	0.26

Table 6: Material parameters of traction wheel.

Material	**QT-600-3**
Young’s modulus	1.69×10^5 MPa
Yield strength	3.70×10^8 MPa
Tensile strength	6.36×10^2 MPa
Density	7.12×10^3 kg/m^3
Poisson’s ratio	0.286
Hardness	240–245 HB

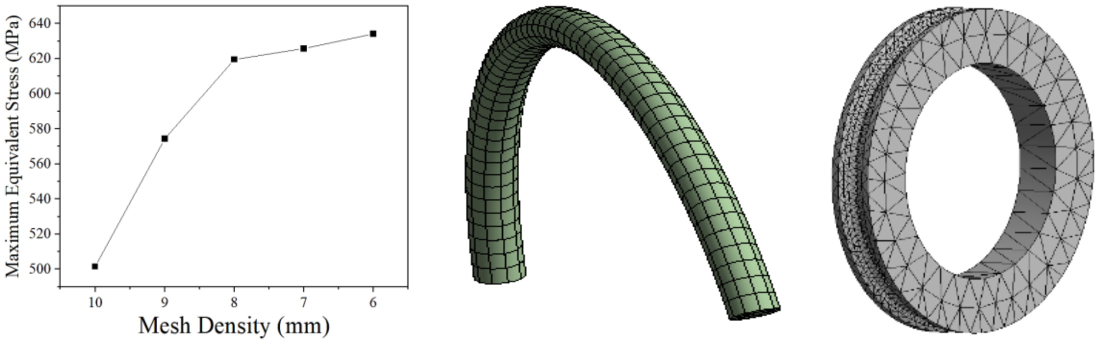

(a) (b) (c)

Figure 11: Grid division. (a) Relationship between mesh density and equivalent stress; (b) Wire rope meshing; (c) Traction wheel meshing.

The operation of the traction elevator adopts the principle of balance at both ends and starts to drive the traction wheel through the motor. After running, the friction between the steel wire rope and the traction wheel drives the elevator car to move up and down, and the opposite side of the heavy block does relative movement. To better study the traction performance and fatigue life of the traction wheel, only the conditions of the traction system under normal loading conditions are considered. Given some analysis premises below, the 3D model is constructed with a traction ratio of 1:1, and the friction of the steel wire rope on the guide wheel is ignored. The moment of inertia of the traction wheel is not large and has no significant impact on the mechanical simulation results; therefore, it is ignored.

Figure 12 shows the relationship curve between the car speed and time under normal loading operation conditions of the traction elevator.

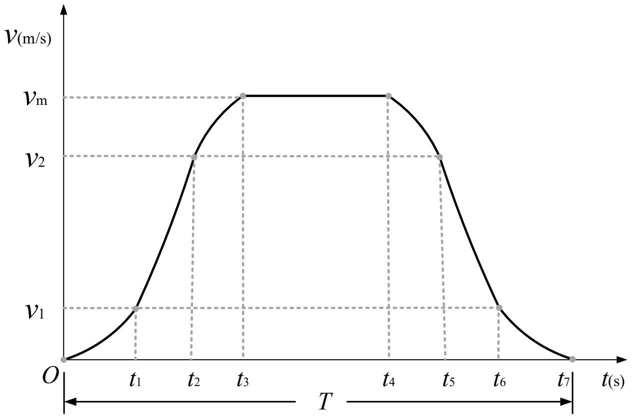

Figure 12: Relationship curve between car speed and time under normal loading and operation conditions.

During the normal operation of the tractor, the tractor wheel undergoes several external loads, such as radial pressure and tangential friction caused by the contact between the steel wire rope and the wheel groove of the tractor, dynamic load or impact load generated during the startup and braking process of the tractor, thermal stress caused by friction heat generated during the braking process, torsional force caused by the rotation of the tractor wheel driven by the tractor, and its own gravity. Among them, the radial pressure and tangential friction are the main loads that have the most significant impact on the groove strength of the traction wheel, which is due to the tension of the wire rope.

The tension at both ends of the wire rope is the lifting-side tension and the lowering-side tension, and the calculation methods for the two are different. The lifting-side tension F_1 and lowering-side tension F_2 are expressed as follows:

$$\begin{cases} F_1 = (g_n + a)(Q + Q_Z + NP_k L_1 + nq_k L_2) \\ F_2 = (g_n - a)(Q_Z + NP_k L_2 + nq_k L_1) \end{cases} \tag{16}$$

In Equation (16), g_n is the acceleration of gravity; a is the acceleration of lifting; Q is the lifting load. To improve the car quality, N and n are the numbers of lifting and balancing ropes, respectively. The unit length quality of lifting wire rope and balancing rope, respectively, L_1 and L_2, are the suspension lengths of the rope on both sides of the light and heavy hauler wheels, respectively.

The elastic creep occurs during the work of the wire rope; the friction factor is μ, and the tension value changes exponentially in the process of decreasing, in line with the Euler formula. At that time, the obtained θ is its creep angle α. The wire rope is tightly pressed on the wheel groove under the tension of both sides, and the tension of each point of the wire rope is equal. The traction wheel model is simplified from six slots to a single slot. Its radial pressure F can be obtained as follows:

$$F = \frac{F_2 e^{\mu\alpha}}{N} \tag{17}$$

According to the friction theorem, the tangential friction force fa of the wire rope acting on the wheel groove can be obtained as follows:

$$f_a = \mu \cdot \frac{F_2 e^{\mu\alpha}}{N} \tag{18}$$

To facilitate loading, a column coordinate system was built on the model with a traction wheel instead of a Cartesian coordinate system. The *x*-, *y*-, and *z*-directions are the radial, tangential, and axial directions of the traction wheel, respectively. The loading of the traction wheel in ANSYS mainly includes the radial pressure of the wire rope on the traction wheel, tension on both sides of the wire rope, and gravity of the traction wheel. The tangential friction between the wire rope and the wheel groove depends on the radial pressure; therefore, only the friction factor μ of the contact between the wire rope and wheel groove is set.

According to the actual acceptance of the traction wheel, the central axis of the traction wheel is tightly connected to the traction machine, and only the rotating motion is about the axis; therefore, a counterclockwise rotation speed is applied to the central axis of the traction wheel. The loading and boundary constraint models of the traction wheel and wire rope under normal loading conditions are illustrated in Figure. 13.

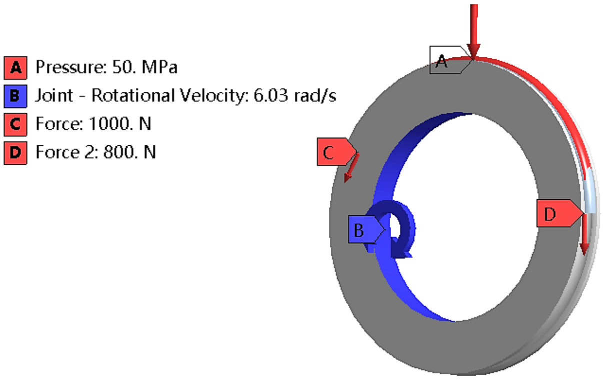

Figure 13: Load and boundary constraints.

4.2 Post-processing of Finite Element Analysis

To study the stress characteristics and fatigue life of traction wheels with different degrees of wear, the transient stress fields of traction wheels with no wear, slight wear, safe wear, and dangerous wear were simulated according to the reconstructed 3D model of traction wheels.

Regarding the elevator traction wheel, which is the key research object of this study, under normal use and maintenance conditions, the wear failure of the traction wheel was mainly caused by the wheel groove. To clarify the simulation results, the two sides of the wheel groove in contact with the wire rope were selected during the postprocessing stage. Figure 14 shows the equivalent stress cloud diagram obtained.

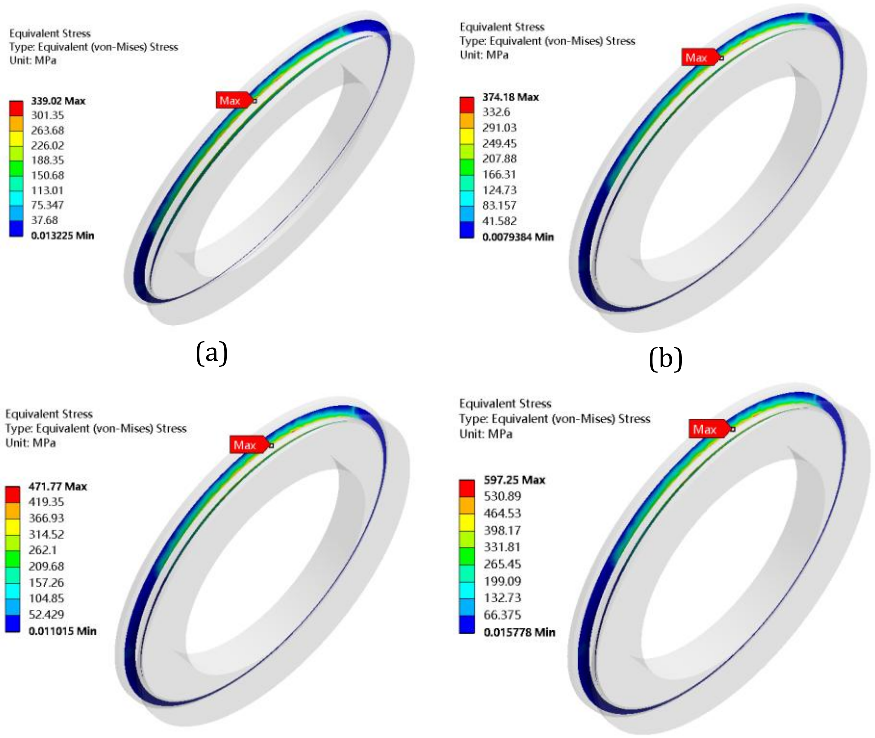

(a) (b)

(c) (d)

Figure14: Equivalent stress nephogram of wheel grooves with different wear degrees. (a) unworn (δ=0mm); (b) Light wear (δ=0.11mm); (c) Safety wear (δ=0.31mm); (d) Dangerous wear (δ=0.72mm).

As shown in Figure 15, most of the stress in the groove of the traction wheel is concentrated in the area in contact with the steel wire rope, particularly on the side with the greater tension of the steel wire rope. This is because, with the rotational movement of the traction wheel to the side with greater tension of the steel wire rope, this side of the wheel groove bears more tension generated by the steel wire rope creep, resulting in a greater impact on the radial pressure of the wheel groove than that on the side with less tension. The maximum equivalent stress of the wheel groove also exists in this area. The maximum equivalent stress of the wheel groove of the traction wheel corresponding to the wear amounts of 0 mm, 0.18 mm, 0.31 mm, and 0.72 mm is 340 MPa, 378 MPa, 481 MPa, and 619 MPa, respectively. Among them, the difference in stress between the wheel groove of the tractor wheel without wear and the wheel groove of the tractor wheel with slight wear is the smallest, and with the deepening of the wear degree, the transient stress value of the wheel groove of the tractor wheel also increases. The higher the wear degree, the greater the change range of the transient stress value. After the tractor wheel reaches the severe wear stage, the wear amount of the wheel groove increases sharply, and the wear resistance of the wheel groove decreases significantly.

A comparative analysis revealed that the maximum equivalent stress of the unworn traction sheave in this study deviated by only 9.76% from findings reported in literature under comparable conditions (Shen et al., 2024). In both instances, the maximum equivalent stress was consistently located at the notch of the pulley groove. Discrepancies in traction sheave diameter, wire rope diameter, and groove opening angle may have contributed to this error, impacting the contact pressure between the wire rope and the traction sheave.

4.3 Fatigue Life Prediction of Traction Wheel

During friction between the steel wire rope and traction wheel, the maximum equivalent stress of the traction wheel increases with an increase in the amount of wheel groove wear. When the maximum equivalent stress of the wheel groove exceeds the yield limit of the material, the friction contact area between the steel wire rope and wheel groove undergoes plastic deformation, which leads to tiny cracks on the surface under the action of continuous accumulation. Subsequently, it expands along the vertical direction of the principal stress, and fatigue failure of the material occurs. During elevator operation, the steel wire rope always slides along the two sides of the wheel groove under the action of the car on both sides and the counterweight. The direction of friction generated is the radial direction of the traction wheel; therefore, the main stress of the fatigue failure of the wheel groove is the radial friction force, and the expansion direction of the surface microcrack is the axial direction perpendicular to the radial direction.

After determining that the fatigue failure of the traction wheel was caused by the action of the steel wire rope in the radial direction of the traction wheel, microcracks generated by the accumulated plastic deformation of the material expanded along the axial direction of the traction wheel. To predict the fatigue life of an elevator traction wheel, the first fatigue failure location of the traction wheel, that is, the location of the maximum equivalent stress, must be identified. Fig. 15 shows a cloud map of the maximum equivalent stress distribution under the operating conditions of the traction wheel elevator. The maximum equivalent stress appeared in the side area of the traction wheel groove. Although the fatigue life analysis of traction wheels with different wear degrees should be conducted separately, because the rope will not contact the area outside the groove of the traction wheel before the failure of the traction wheel, the stress situation of the traction wheel with different wear degrees is essentially the same, and the dangerous parts of the fatigue damage are also the same. Therefore, selecting a wear-traction wheel is crucial to determine dangerous parts.

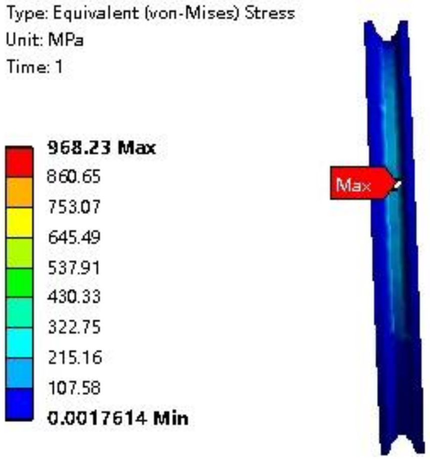

Figure 15: Maximum equivalent stress distribution cloud map of traction wheel.

As early as the 1950s, domestic and foreign scholars examined the fatigue life of parts. Subsequently, after continuous improvement by numerous researchers, the relationship between the total failure strain energy, plastic strain energy, and the number of fatigue limit cycles of materials was established based on the Manson–Coffin fatigue model. Combined with the linear cumulative damage theory of fatigue, when the plastic strain energy of multiple cycles accumulates to the total failure strain energy, fatigue failure of parts occurs. The formula for calculating the number of contact fatigue cycles of parts is as follows:

$$N = \frac{1+n^{'}}{1-n^{'}} \cdot \frac{GW_R\left(2\tau_s - \mu\sigma_{\max}\right)}{0.125\sigma_{\max}^2\tau_s} \tag{19}$$

In Equation (19), *n'* is the cyclic hardening index of shear stress, *G* is the shear modulus of the material, W_R is the total shear plastic strain energy, τ_s is the shear strength of the material, μ is the friction coefficient of the contact surface, and $\sigma_{\max}$ is the maximum equivalent stress.

In rotating the traction wheel in one circle, the speed of the traction wheel is *v*, the radius of the pitch circle is *R*, and the time required to rotate the traction wheel in one circle is

$$t = \frac{2\pi R}{v} \tag{20}$$

The effective contact time between the wire rope and traction wheel is the time at which the traction wheel turns over the package angle. One circle is equivalent to one contact-stress cycle for the internal stress of the wheel groove. Therefore, when the number of rotation cycles *n* of the traction wheel under normal loading conditions is equal to the number of contact fatigue cycles *N* of the traction wheel groove, the rotation time *T* of the traction wheel is the limit service life of the traction wheel, and the expression for the number of rotating circles *n* of the traction wheel is

$$n = \frac{vT}{2\pi R} \tag{21}$$

From Equations (19) and (21), the expression for the ultimate service life *T* of the traction wheel can be obtained, as shown in Equation (22).

$$T = \frac{2\pi R}{v} \cdot \frac{1+n^{'}}{1-n^{'}} \cdot \frac{GW_R\left(2\tau_s - \mu\sigma_{\max}\right)}{0.125\sigma_{\max}^2\tau_s} \tag{22}$$

As the production material of the traction wheel is QT-600-3 ductile iron, the performance parameters of the QT-600-3 ductile iron can be obtained by consulting the data and combining them with the relevant parameters of the traction wheel to obtain the parameters required for the fatigue life calculation (Table 7).

Based on the contact mechanical simulation results, the maximum equivalent stress of the wheel groove of the traction wheel with corresponding wear amounts of 0 mm, 0.11 mm, 0.31 mm, and 0.72 mm is 340 MPa, 378 MPa, 481 MPa, and 619 MPa, respectively. The above fatigue life calculation parameters are substituted into Equation (22) for calculation, and the specific residual fatigue lives of the wear traction wheel, which are 1.69×108 s, 1.33×108 s, 7.69×107 s, and 4.20×107 s, respectively, can be obtained.

Table 7: Parameters related to fatigue life calculation.

Parameter name	Parameter symbol	Parameter value
Pitch circle radius of traction wheel	R	520mm
Linear speed of traction wheel rotation	v	2m/s
Shear cycle hardening index	n'	0.148
Shear modulus	G	41.34GPa
Cyclic hysteresis energy of total shear stress	WR	1.63×107J
Shear strength	τ_s	192MPa

Assuming that the traction elevator works for an average of 365 days per year and runs for 12 h per day, the remaining life T_P of the worn traction wheel can be calculated using Equation (23) in years.

$$T_P = \frac{T}{60\times 60\times 12\times 365} \tag{23}$$

The remaining lives of the traction wheel corresponding to the four wear amounts above were 10.7 years, 8.5 years, 4.9 years, and 2.7 years, respectively. The relevant data show that, according to the market survey, the service life of the traction wheel is generally 10–15 years, and the calculated life of the nonworn traction wheel is 10.7 years. Life prediction results are consistent with the market research results, verifying the accuracy of the life prediction method. With an increase in the degree of wear, the remaining life of the tractor wheels decreased. Fig. 16 shows the fatigue life curve of the tractor wheel with the maximum equivalent stress value. When the maximum equivalent stress is zero, the fatigue life of the tractor wheel is infinite. When the maximum equivalent stress is infinity, the fatigue life of the tractor wheel is zero.

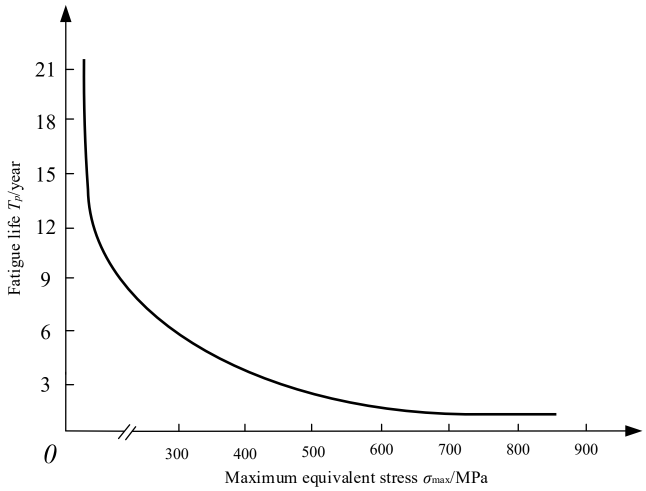

Figure 16: Fatigue life curve of traction wheel.

5.0 CONCLUSION

This study analyzed the influence of groove wear on the traction performance of a traction wheel and realized the fatigue life prediction of a worn traction wheel. The effects of friction coefficient f and envelope angle α on the groove wear were analyzed based on the traction coefficient relation of the tractor wheel, and the traction performance of the tractor wheel with different wear degrees was analyzed based on the 3D reconstruction model of the tractor wheel. The results showed that the groove wear primarily affected the friction coefficient but minimally affected the envelope angle of the tractor wheel. When the wear amount reached 1.33 mm, the friction coefficient of the tractor wheel was affected. Drag coefficient G did not change afterward. Based on the reconstructed tractor wheel model, the transient stress fields of four types of tractor wheels with different degrees of wear were analyzed using the finite element simulation method. The maximum equivalent stress of the wheel groove of the tractor wheel with corresponding wear amounts of 0 mm, 0.18 mm, 0.31 mm, and 0.72 mm was 340 MPa, 378 MPa, 481 MPa, and 619 MPa, respectively. Finally, the fatigue life prediction model of the traction wheel was established, and the remaining fatigue life of the traction wheel corresponding to the four wear degrees was 10.7 years, 8.5 years, 4.9 years, and 2.7 years, respectively. Thus, the fatigue life of the worn traction wheel continuously shortened with increasing wear amount of the wheel groove, and the change in amplitude was the same. Therefore, studying the traction performance and fatigue life of worn traction wheels using a 3D reconstruction method was useful.

ACKNOWLEDGEMENT

This study was financially supported by Guangxi Market Supervision Administration Science and Technology Project (Grant No. GXSJKJ2023-13), the Guangxi Key Research and Development Program (AB22035048), Scientific and Technological Planning Project of State Administration for Market Regulation (2023MK153).

REFERENCES

Birt, E. A., Jones, L. D., Nelson, L. J., et al. (2006). NDE corrosion metrics for life prediction of aircraft structures. Insight - Non-Destructive Testing and Condition Monitoring, 48(3), 139–145.

Bošnjak, S., Arsić, M., Savićević, S., et al. (2016). Fracture analysis of the pulley of a bucket wheel boom hoist system. Eksploatacja i Niezawodnosc – Maintenance and Reliability, 18(2), 155–163.

Fleishman, S., Drori, I., & Cohen-Or, D. (2003). Bilateral mesh denoising. ACM Transactions on Graphics, 22(3), 950–953.

Guarda, A., Bivouacs, M., Rodrigues, N. M., et al. (2017). Improving point cloud to surface reconstruction with generalized Tikhonov regularization. In Proceedings of the 19th International Workshop on Multimedia Signal Processing (pp. 1–6).

Li, J., Zhang, Z., Meng, Z., et al. (2019). Tunnel boring machine cutterhead crack propagation life prediction with time integration method. Advances in Mechanical Engineering, 11(6), 168781401985345.

Li, M., Liu, Z., & Lin, Z. (2006). Parametric reconstruction of surface fragments based on square distance function. Journal of Xi'an Jiaotong University, 40(9), 1053–1057.

Ma, J. (2011). Surface reconstruction from unorganized point cloud data via progressive local mesh matching. Electronic Thesis and Dissertation Repository.

Molent, L., Spagnoli, A., Carpinteri, A., et al. (2017). Using the lead crack concept and fractal geometry for fatigue lifing of metallic structural components. International Journal of Fatigue, 102, 214–220.

Morse, B. S., Yoo, T. S., Chen, D. T., et al. (2001). Interpolating implicit surfaces from scattered surface data using compactly supported radial basis functions. In Proceedings of the International Conference on Shape Modeling and Applications (pp. 89–98).

National Standard of the People's Republic of China. (2003). Safety rules for the construction and installation of elevators (GB 7588-2003). Standards Press of China.

Papas, N., Tsongas, K., & Tzetzis, D. (2022). Investigation of traction sheave failure: Experimental and finite element analysis. Journal of Failure Analysis and Prevention, 22(2), 595–608.

Paris, P. C., & Palin-Luc, T. (2009). The behavior of statically indeterminate structural members and frames with cracks present. Engineering Fracture Mechanics, 76(12), 1920–1929.

Savchenko, V., Pasko, A., Okine, G., et al. (1995). Function representation of solids reconstructed from scattered surface points and contours. Computer Graphics Forum, 14(4), 181–188.

Shen, Y., Jin, Z., Dong, L., et al. (2024). Contact stress analysis of elevator traction wheel rope groove and wire rope under different structural parameters. China Elevator, 35(8), 5–7.

Shi, X., & Jia, S. (2021). Design of on-line detecting device for groove wear of elevator traction wheel. Journal of Physics: Conference Series, 2095(1), 012073.

Taubin, G. (1995). A signal processing approach to fair surface design. In Proceedings of the 22nd Annual Conference on Computer Graphics and Interactive Techniques (pp. 351–358).

Tao, S., Liu, X., Li, B., et al. (2018). 3D data denoising method based on density clustering and voting discrimination. Application Research of Computers, 35(2), 619–623.

Wang, C., Xiang, Z., & Liu, J. (2010). Application of 3D laser scanning technology in 3D reconstruction of cultural relics. Urban Geotechnical Investigation & Surveying, 6, 67–70.

Wang, H., Huang, M., Gao, X., et al. (2021). Dynamic wear identification of elevator's traction sheave based on multiple acoustic emission information fusion. Journal of the Brazilian Society of Mechanical Sciences and Engineering, 43(6), 290.

Wang, P. S., Liu, Y., & Tong, X. (2016). Mesh denoising via cascaded normal regression. ACM Transactions on Graphics, 35(6), 1–12.

Wu, Y. L. (2003). Study on the elastic modulus of steel wire rope. Fujian Forestry Science and Technology, 30(3), 62–64.

Xu, J., Yu, M., & Zheng, Y. (2008). Briefing on terrestrial 3D laser scanner. Geotechnical Investigation and Surveying, 12, 31–34.

Zhang, D., Han, X., & Han, H. (2017). Global parametric surface reconstruction method based on point cloud. Computer Engineering and Design, 38(7), 1911–1916.

Zhang, H., Wu, C., Zhang, J., et al. (2015). Variational mesh denoising using total variation and piecewise constant function space. IEEE Transactions on Visualization and Computer Graphics, 21(7), 873–886.

Zhu, Y., Kang, B., Li, H., et al. (2012). An improved point cloud data reduction method. Journal of Computer Applications, 32(2), 521–523, 544.

Zou, B., Qiu, H., & Lu, Y. (2020). Point cloud reduction and denoising based on optimized down-sampling and bilateral filtering. IEEE Access, 8, 136316–136326.